(Sub)millimeter Dust Polarization of Protoplanetary Disks from Scattering by Large Millimeter/Centimeter-Sized Irregular Grains

Zhe-Yu Daniel Lin,[1]★ Zhi-Yun Li,[1] Haifeng Yang,[2] Olga Muñoz,[3] Leslie Looney,[4] Ian Stephens,[5] Charles L. H. Hull,[6,7]† Manuel Fernández-López,[8] and Rachel Harrison[4]

[1]*Department of Astronomy, University of Virginia, 530 McCormick Rd., Charlottesville, Virginia 22904, USA*
[2]*Kavli Institute for Astronomy and Astrophysics, Peking University, Yi He Yuan Lu 5, Haidian Qu, Beijing 100871, People's Republic of China*
[3]*Instituto de Astrofísica de Andalucía, CSIC Glorieta de la Astronomía s/n, E-18008 Granada, Spain*
[4]*Department of Astronomy, University of Illinois, 1002 W Green St., Urbana, IL 61801, USA*
[5]*Department of Earth, Environment and Physics, Worcester State University, Worcester, MA 01602, USA*
[6]*National Astronomical Observatory of Japan, NAOJ Chile Observatory, Alonso de Córdova 3788, Vitacura, Santiago, Chile*
[7]*Joint ALMA Observatory, Alonso de Córdova 3107, Vitacura, Santiago, Chile*
[8]*Instituto Argentino de Radioastronomía (CCT-La Plata, CONICET; CICPBA), C.C. No. 5, 1894, Villa Elisa, Buenos Aires, Argentina*

Accepted XXX. Received YYY; in original form ZZZ

ABSTRACT

The size of dust grains plays a fundamental role in determining the physical and chemical processes in circumstellar disks, but observational constraints of grain size, a, remain challenging. (Sub)millimeter continuum observations often show a percent-level polarization parallel to the disk minor axis, which is generally interpreted as coming from scattering by $\sim 100\mu$m-sized spherical grains (with a size parameter $x \equiv 2\pi a/\lambda < 1$, where λ is the wavelength). Larger spherical grains (with x greater than unity) would produce polarization parallel to the disk major axis, in contradiction to the observed pattern. The inferred grain size of $\sim 100\mu$m is in tension with the opacity index β that point to larger mm/cm-sized grains. However, grains are expected to be non-spherical and irregular under realistic conditions. Here we investigate the scattering-produced polarization by large irregular grains with x much larger than unity with optical properties obtained from laboratory experiments. Using the radiation transfer code, RADMC-3D, we simulate polarization images and find that large irregular grains still produce polarization parallel to the disk minor axis. Our results suggest that scattering grains at (sub)millimeter wavelengths in disks are not limited to $\sim 100\mu$m, but can easily have millimeter sizes or even larger, thus alleviating the long-standing tension between the grain sizes inferred from scattering and other means. Additionally, if large irregular grains are not settled to the midplane, their strong forward scattering can produce asymmetries between the near and far side of an inclined disk, which can be used to infer their presence.

Key words: polarization – protoplanetary disks – circumstellar matter

1 INTRODUCTION

Dust in circumstellar disks only holds about 1% of the total disk mass, yet it plays a key role in shaping disk properties and serves as the fundamental building blocks of planets. One of the most relevant properties of dust is its size. The growth to planets directly requires the aggregation of grains from submicron sizes inherited from the interstellar medium to kilometer-sized planetesimals and eventually to planets (e.g. Bitsch et al. 2015; Drążkowska & Dullemond 2018). The grains dominate the opacity, which is sensitive to grain size (e.g., Draine 2006; Birnstiel et al. 2018). As a result, grains and how the various sizes distribute in the disk affect the temperature structure (e.g. D'Alessio et al. 2001; Inoue et al. 2009; Williams & Cieza 2011) and the multiwavelength observational appearance of disks (e.g. Dong et al. 2018; Huang et al. 2020; Sierra et al. 2021). The grain sizes directly impact the chemistry of disks because of its dependence on temperature (e.g. Gavino et al. 2021) and dust opacity at UV which affects photodissociation (e.g. Cleeves et al. 2011), and also because surface chemistry relies on the grain surface area (e.g Harada et al. 2017). The dynamics and evolution of disks depend on the grain sizes which govern how coupled the grains are to the gas and also the level of ionization (e.g. Hu et al. 2021). Despite the importance of dust grain size, it has been difficult to directly constrain their sizes from observations.

One way to measure the grain size of disks is through (sub)millimeter continuum polarization. With the tremendous sensitivity of the Atacama Large Millimeter/submillimeter Array (ALMA), (sub)millimeter polarized images have been resolved for many disks. Grains scatter radiation, and the scattered radiation becomes polarized. Since the grains scatter its own thermal radiation at the (sub)millimeter wavelengths, it is often called self-scattering (Kataoka et al. 2015). A characteristic feature of polarization due to self-scattering is the unidirectional polarization that is parallel to the minor axis of inclined disks (Yang et al. 2016; Kataoka et al. 2016). The majority of the observed polarization images are ~ 1% polarized and show the unidirectional polarization feature, especially at relative

★ Jefferson Fellow. E-mail: zdl3gk@virginia.edu
† NAOJ Fellow

short wavelength ALMA Bands, like Bands 6 and 7 (e.g. Stephens et al. 2017; Bacciotti et al. 2018; Hull et al. 2018; Lee et al. 2018; Dent et al. 2019; Sadavoy et al. 2019; Stephens et al. 2020; Aso et al. 2021; Harrison et al. 2021). To efficiently produce polarization, the grain size, a, must not be much smaller than the observing wavelength, λ, (Kataoka et al. 2015), but grains much larger than the wavelength can cause the polarization to become parallel to the disk major axis (Yang et al. 2016). In other words, the size parameter, $x \equiv 2\pi a/\lambda$, should be of order unity. As a result, polarization is deemed sensitive to grain size and the majority of detected polarization images have been taken as evidence for grains of $\sim 100\mu$m.

Another way to estimate grain sizes is through the wavelength dependence of opacity. For grains with absorption opacity that goes as $\kappa_{\rm abs} \propto \nu^{\beta}$, the opacity index β depends on the grain size (Draine 2006). For the interstellar medium, the small grains ($\sim 0.1\mu$m) have $\beta \sim 1.7$ (Weingartner & Draine 2001). The typically inferred β of disks at millimeter wavelengths is ~ 1 or lower (e.g. Beckwith et al. 1990; Ubach et al. 2012; Sheehan & Eisner 2018; Tobin et al. 2020; Lin et al. 2021). At face value, the low β suggests mm/cm-sized grains (e.g. Draine 2006; Testi et al. 2014) which directly contradicts the size inferred from polarization.

The orders of magnitude discrepancy between 100 μm versus the mm/cm regime can heavily affect the interpretation of the physical and chemical properties of the disk given the importance of the grain size. In this paper, we demonstrate that the perceived accuracy of polarization measurements in constraining the grain size is due to the strict assumption of spherical grains. Since grains coagulate to form larger grains, the shape of grains is expected to be irregular (e.g. Krause & Blum 2004; Ormel et al. 2007; Blum & Wurm 2008). Though the assumption of spherical grains is largely based on its numerical simplicity (calculated from Mie theory), the scattering properties of spherical grains becomes drastically different from those of irregular grains once the size becomes comparable to the size of the observing wavelength, as predicted from more sophisticated numerical techniques (e.g. Shen et al. 2008, 2009; Kirchschlager & Wolf 2013, 2014; Tazaki et al. 2016; Tazaki & Tanaka 2018; Tazaki et al. 2019; Kirchschlager & Bertrang 2020) and shown from experimental measurements (e.g. Muñoz et al. 2011, 2021).

In this paper, we use scattering matrices measured from the Instituto de Astrofísica de Andalucía (IAA) Cosmic Dust Laboratory (CoDuLab; Muñoz et al. 2011, 2012, 2021) as illustrative samples of the scattering matrix when the size parameter x is much larger than unity to simulate the (sub)millimeter disk polarization. By using the experimentally measured scattering matrices, we can consider grains with size parameters up to 575 in this paper, which is larger than what current numerical techniques can readily achieve. In Section 2, we briefly describe the properties of the experimental dust samples and disk model setup. We use the Monte Carlo radiative transfer code RADMC-3D[1] to simulate the polarization images at millimeter wavelengths (Dullemond et al. 2012). Section 3 presents the simulated polarization images comparing the use of laboratory measured scattering matrix and the Mie calculations. We show that irregular grains with large size parameters can still produce polarization parallel to the disk minor axis. Since large grains exhibit strong forward scattering, we also show how forward scattering affects the polarization image. Section 4 offers a discussion of the implications and the results are summarized in Section 5.

[1] RADMC-3D is available at https://www.ita.uni-heidelberg.de/~dullemond/software/radmc-3d/

2 SIMULATION SETUP

2.1 Dust Model

We use the experimental scattering matrix for a set of forsterite (in the form of $(\mathrm{Mg,Fe})_2\,\mathrm{SiO_4}$ and $\mathrm{Mg_3Si_2O_5(OH)_4}$) samples presented by Muñoz et al. (2021). The elements of the scattering matrix F_{ij} depend on the physical properties of the grain, such as shape, size and composition, and the direction of scattering (e.g., the angle form by the directions of the incident and scattered beams). In the case of randomly oriented particles as is the case in the CoDuLab experiment, all scattering planes are equivalent and the scattering direction is fully described by the scattering angle θ. The 4×4 scattering matrix $\mathbf{F}$ becomes a block diagonal and is defined by

$$\begin{pmatrix} I_s \\ Q_s \\ U_s \\ V_s \end{pmatrix} \propto \begin{pmatrix} F_{11} & F_{12} & 0 & 0 \\ F_{12} & F_{22} & 0 & 0 \\ 0 & 0 & F_{33} & F_{34} \\ 0 & 0 & -F_{34} & F_{44} \end{pmatrix} \begin{pmatrix} I_i \\ Q_i \\ U_i \\ V_i \end{pmatrix} \tag{1}$$

where (I_i, Q_i, U_i, V_i) and (I_s, Q_s, U_s, V_s) are the Stokes parameters of the incoming and scattered light respectively. For unpolarized incident light (I_i,Q_i,U_i,V_i)=$(1, 0, 0, 0)$), the $F_{11}(\theta)$ function is proportional to the flux of the scattered light and is called the phase function. Also, for unpolarized incident light, the ratio $-F_{12}(\theta)/F_{11}(\theta)$ is called the degree of linear polarization of the scattered light, hereafter DLP

Due to the limited amount of grain samples, the measurements are limited to the $F_{11}(\theta)$, $F_{12}(\theta)$, and $F_{22}(\theta)$ scattering matrix elements and $F_{33}(\theta)$, $F_{34}(\theta)$, and $F_{44}(\theta)$ are not measured. We supplement the missing scattering elements by the following. Motivated by laboratory measured F_{33} elements of irregular grains of olivine from Muñoz et al. (2000) (see their Fig. 5), we set $F_{33}(\theta) = (-0.45\theta + 1)F_{11}(\theta)$ with θ in radians. We do not consider circular polarization and set F_{34} and F_{44} to zero. Given that the ratio F_{34}/F_{11} of irregular grains from Muñoz et al. (2000) is $\sim 10\%$ at most, circular polarization is at least an order of magnitude less than linear polarization which makes the impact marginal. Since there is a lack of confident detection in Stokes V in disks (e.g. Stephens et al. 2017), it is beyond the scope of this paper.

The bulk forsterite sample was processed for producing various size distributions namely XS, S, L and XL. Table 1 lists the effective size parameter ($x_{\rm eff}$) of each sample at the experimental wavelength (λ = 514 nm) which was used to measure the scattering properties in the laboratory. The corresponding equivalent effective radii $a_{\rm eff}$ at 1 mm wavelength, which is the wavelength we use for the simulations, are also presented by fixing the effective size parameter through $a_{\rm eff} = x_{\rm eff} \times 1\mathrm{mm}/(2\pi)$. Note that at 1 mm wavelength, the samples XS and S are representative of mm-sized grains, while the samples L and XL are in the centimeter and decimeter size regime.

Since the experimental scattering matrices do not cover the full angular extent (3° to 177°), we use the synthetic scattering matrix whose scattering angle θ is defined from 0° to 180° to adequately apply the results from experimental scattering matrix to radiation transfer. The extrapolation of the scattering matrix elements is based on the technique described by Escobar-Cerezo et al. (2017) and further improved by Gómez Martín et al. (2021).

To compare the disk images produced from experimental scattering matrix and from Mie calculations, we need the absorption opacity $\kappa_{\rm abs}$ and the scattering matrix. However, the experimental data does not have $\kappa_{\rm abs}$ and its scattering matrix is a relative quantity which means the absolute values of each element are unknown. Thus, for each experimental sample, we assign the same $\kappa_{\rm abs}$ and scattering opacity $\kappa_{\rm sca}$ from Mie calculations using the respective grain size

distribution[2]. To produce smooth profiles from Mie calculations, we refine the grain size bins by linearly interpolating the experimental size distributions; otherwise, the coarse grain size bins measured from the laboratory produces severe oscillations when implementing Mie calculations. We scale F_{11} of the experimental data based on

$$\kappa_{\rm sca} \equiv 2\pi \int F_{11} \sin\theta d\theta. \quad (2)$$

such that $\kappa_{\rm sca}$ is equal to its Mie counterpart. For convenience, the extinction opacity $\kappa_{\rm ext}$ is defined as $\kappa_{\rm ext} \equiv \kappa_{\rm abs} + \kappa_{\rm sca}$ and the albedo is $w \equiv \kappa_{\rm sca}/(\kappa_{\rm abs}+\kappa_{\rm sca})$. Note that in Section 2.2 below, we define the surface density in terms of the optical depth and as such $\kappa_{\rm ext}$ cancels out. This means the absolute difference in opacity across the different samples would not matter since it is the optical depth (surface density multiplied by $\kappa_{\rm ext}$) that determines the radiation transfer results.

Mie calculations also require a refractive index $m = n + ik$ where n and k are the real and imaginary parts respectively. We use $1.65 + 10^{-5}i$ for the forsterite material at the experiment wavelength (Huffman & Stapp 1973) to directly compare with the experimental scattering matrix. However, we note that the experimental k can be a few orders of magnitude lower than the k at millimeter wavelengths from commonly adopted material for disks, such as water-ice, silicates, or organics (e.g. Pollack et al. 1994; Draine 2003a; Birnstiel et al. 2018), which we discuss in Section 4.2.

While conducting the Monte Carlo simulation, most photons are scattered in the forward direction given the large forward scattering peak of the large grains for the experimental samples (and also the Mie calculations described below). However, this leads to difficulty in obtaining smooth images since most of the radiation is directed in the forward direction which is not polarized and only the small portion of photons that are side-scattered contribute polarization. Given that large forward scattering is effectively no scattering at all, we truncate the forward scattering peak at 1° by setting $F_{ij}(\theta < 1^\circ) = 0$ to obtain smooth images with achievable computational time (see e.g. Nakajima & Tanaka 1988; Iwabuchi 2006). The scattering opacity is calculated from F_{11} after truncation. We have experimented with different choices of the truncation angles and found quantitatively similar results (see Appendix A).

Fig. 1a shows the experimental phase function F_{11} as a function of the scattering angle θ for each of the samples. The element represents the angular distribution of scattered photons. For comparison, we also show F_{11} for Rayleigh scattering which goes as $F_{11} \propto \cos^2\theta + 1$. The experimental F_{11} for each sample shows a strong forward scattering which is different from the Rayleigh limit that has equal forward and backward scattering.

Fig. 1b shows the experimental $-F_{12}/F_{11}$ (i.e., the DLP). Positive values of DLP mean the polarization is perpendicular to the scattering plane. Across all four samples, the DLP curves are roughly bell-shaped with peaks of $\sim 0.1 - 0.2$. The samples XS and S have small but negative polarization for large θ (in the vicinity of back-scattering). The DLP for all four samples are similar to the bell-shaped curve for particles in the Rayleigh limit, except the peak in the Rayleigh limit is 100% polarized.

Fig. 2 compares the laboratory DLP with its respective Mie calculation (see Fig. 9 in Muñoz et al. 2021 for a similar plot). Across all four samples, the Mie calculations are drastically different from the laboratory measurements. Most notably, the Mie calculations do not follow a simple bell shaped curve with the peak at $\theta \sim 90^\circ$. Furthermore, the sign of the Mie DLP are mostly negative, which is the well-known polarization reversal (Kataoka et al. 2015; Yang et al. 2016). In other words, the scattered light will be polarized in the scattering plane as opposed to being polarized perpendicular to the scattering plane for the Rayleigh regime or, evidently, the experimental DLP. The consequences of the differences between the Mie and experimental DLP's will be seen in the disk polarization images in Section 3.1 below.

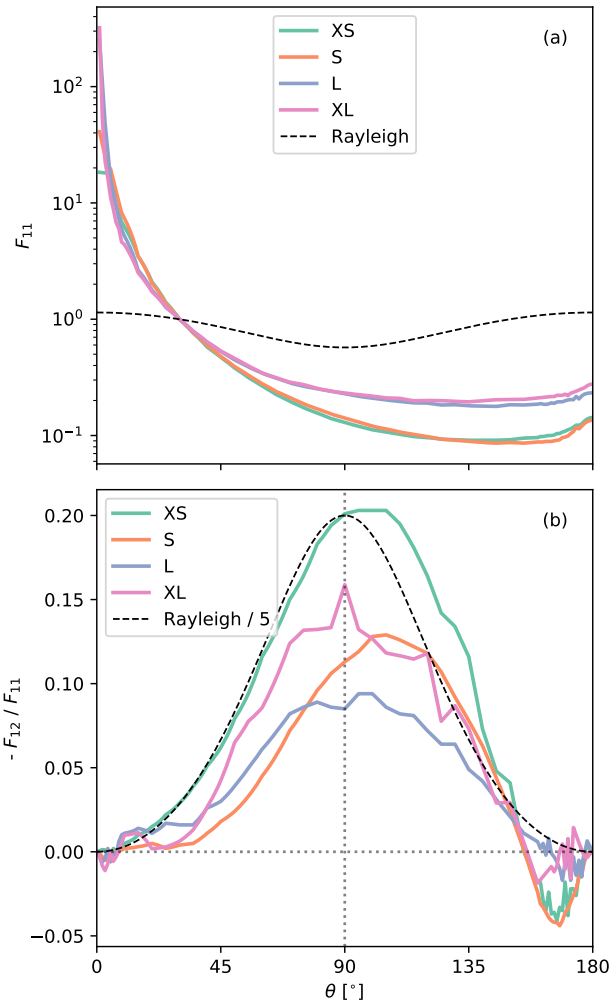

Figure 1. Top: The phase function F_{11} as a function of scattering angle θ for the different samples. The Rayleigh scattering $F_{11} \propto \cos^2\theta + 1$ is also shown as a comparison. For better comparison, each are normalized at $\theta = 30^\circ$ to an arbitrary value of 1. Bottom: The degree of linear polarization (DLP) which is defined as $-F_{12}/F_{11}$ for the different samples. The Rayleigh scattering DLP at $\theta = 90^\circ$ should be 100%, but we scaled it down to 20% for better comparison with the experimental data.

2.2 Disk Model Setup

We consider a fiducial disk model with a dust surface density following a simple prescription (Lynden-Bell & Pringle 1974):

$$\Sigma(R) = \Sigma_c \left(\frac{R}{R_c}\right)^{-\gamma} \exp\left[-\left(\frac{R}{R_c}\right)^{2-\gamma}\right], \quad (3)$$

[2] The Python code for Mie scattering is written by C. Dullemond which is included in the RADMC-3D package. The code is based on the FORTRAN code available at `https://www.astro.princeton.edu/~draine/scattering.html` which originates from Bohren & Huffman (1983).

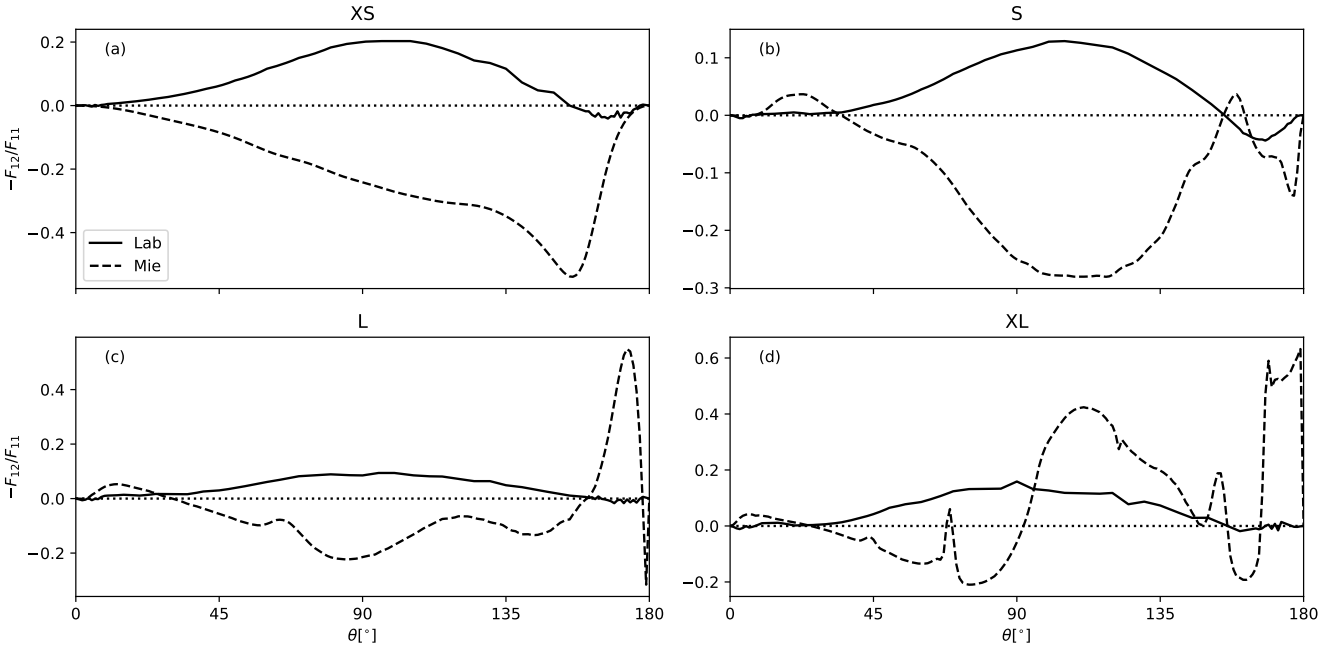

Figure 2. The degree of linear polarization (DLP) defined by $-F_{12}/F_{11}$ curves of the different laboratory samples (solid lines) compared to their corresponding Mie calculations (dashed lines).

Sample	$x_{\rm eff}$	$a_{\rm eff}$ [mm]
XS	4.4	0.70
S	17	2.7
L	43	6.8
XL	575	91.6

Table 1. The measured effective size parameter $x_{\rm eff}$ for each sample and the corresponding effective size $a_{\rm eff}$ scaled to an observing wavelength of 1 mm.

where R is the cylindrical radius, R_c is the characteristic radius, and γ is the exponent that determines the radial power-law and exponential taper. The characteristic surface density is $\Sigma_c = \tau_0/\kappa_{\rm ext}$ where we define τ_0 as the characteristic optical depth in the vertical direction of the disk. The prescription allows us to scale the optical depth through τ_0 directly since the $\kappa_{\rm ext}$ is canceled out with opacity. We fix $R_c = 50$ au as a representative size scale of dust disks (e.g. Andrews 2020; Sheehan et al. 2022). We set $\gamma = -0.2$ motivated by modeling of HL Tau (Kwon et al. 2011, 2015) and to connect to previous studies (Yang et al. 2017). The temperature is vertically isothermal and the radial profile goes as $R^{-0.5}$ with 30 K at 50 au to represent a passively heated disk (e.g. Chiang & Goldreich 1997; Dullemond et al. 2001).

Motivated by vertical hydrostatic equilibrium and dust settling (e.g. Dubrulle et al. 1995), the vertical dust density follows a Gaussian distribution

$$\rho(R,z) = \frac{\Sigma}{\sqrt{2\pi}H}\exp\left[-\frac{1}{2}\left(\frac{z}{H}\right)^2\right] \quad (4)$$

where H is the dust scale height as a function of radius. For simplicity, we adopt a power-law for the dust scale height

$$H(R) = H_0\left(\frac{R}{R_c}\right)^{1.25} \quad (5)$$

where H_0 is the dust scale height at R_c. The prescription allows the freedom to study the effects of the geometrical thickness of the disk by changing H_0.

We use the three-dimensional Monte Carlo radiative transfer code, RADMC-3D to simulate the full Stokes (I, Q, U, V) images. The disk is set at a 45° inclination and each image used 10^9 photons.

3 RESULTS

3.1 Fiducial Model

In this section, we compare the polarization images calculated from the laboratory samples and those from Mie theory. The linear polarized intensity P is defined as $P \equiv \sqrt{Q^2+U^2}$, while the linear polarization fraction is $p_f \equiv P/I$. We first choose $H_0 = 0.5$ au and $\tau_0 = 1$ which represents a geometrically thin and optically thin disk. The chosen dust scale height is small since the millimeter emission of disks are generally observed to be thin, roughly 1% of the radius (e.g. Pinte et al. 2016; Villenave et al. 2020). The value of $\tau_0 = 1$ makes the interpretation simple for this section. We consider a larger optical depth in Section 3.2.

The left column of Fig. 3 shows the polarization fraction and polarization direction images of the disk using the various samples of experimental dust grains. The relative levels of p_f roughly correspond to the relative levels of their maximum DLP in Fig. 1b which is expected given that the albedos for these large grains are nearly equivalent at ~ 0.99. The images show polarization that is parallel to the disk minor axis at the central regions (roughly within the region where the total optical depth is ~ 0.1 traced by the dashed white contour), while the outer regions of the disk show polarization that is more azimuthal. The two features are qualitatively similar to the pattern from Rayleigh scattering where the polarization parallel to the disk minor axis is simply due to inclination and the outer region is expected from radiation anisotropy (e.g. Kataoka et al. 2015; Yang

et al. 2016). This resemblance is expected because the DLP curves of Fig. 1b exhibit similar positive bell-shaped curves (scattered light is polarized perpendicular to the scattering plane) as the Rayleigh scattering approximation.

As a comparison, we show the polarization fraction images using the corresponding Mie theory calculations in the right column of Fig. 3. The most striking result is the 90° offset in the polarization direction at the center of the disk between the lab scattering matrix and Mie calculations. This is true for all the samples considered here. The Mie calculations produce negative DLP (Fig. 1) for these large grains which causes the polarization to become parallel to the disk major axis. Between the Lab and Mie model images for samples XS, S, and L, the outer regions of the disk are perpendicular to each other also because of the opposite sign in the DLP. The outer regions of the Lab and Mie XL sample models are not entirely perpendicular to each other because the DLP of the Mie calculation (Fig. 1d) is mostly opposite when θ is less than $\sim 90°$ (the forward scattering half) while it has the same sign when θ is greater than $\sim 90°$ (the back scattering half). Since radiation mostly travels outward for the outer region, the polarization direction is mostly perpendicular to the Lab counterpart at the near side (bottom half of the image) where most photons are forward scattered, while polarization is mostly parallel to the Lab counterpart at the far side (upper half of the image) where most photons are back scattered.

The level of polarization fraction from Mie calculations also do not resemble the corresponding laboratory samples. The level of polarization of images from laboratory matrices are generally lower than its Mie counterpart. The XS and XL samples have $\sim 0.5\%$ peak polarization, while the S and L samples have $\sim 0.3\%$. The images from Mie calculation have peak levels of polarization at $\sim 0.8\%$ with the XS sample and at $\sim 0.4\%$ with the XL sample. The largest grain sizes have the lowest level of polarization, which is different from the images using laboratory matrices.

3.2 Effects of Strong Forward Scattering

The most striking feature from Section 3.1 is the difference in the polarization angle between the calculations using lab measurements and Mie results since the DLP for the large irregular grains in consideration is more similar to the Rayleigh scattering behavior. However, if grains are indeed large, we would expect large forward scattering which is drastically different from the Rayleigh limit (Fig. 1).

In the limit where photons travel radially in the midplane of the disk, we would expect photons at the near side of the inclined disk to be forward scattered to reach the observer as opposed to the far side where photons will be more back scattered. Given that the forward scattering peak of the phase function F_{11} is a few orders of magnitude larger than side-scattering or back-scattering, one may expect scattering by large irregular grains to potentially cause a significant near-far side asymmetry. In this section, we show that the near-far side asymmetry can be significant if the scattering dust disk is geometrically thick, but the asymmetry almost disappears for a geometrically thin disk. As we explain below, this is an extension from the near-far side asymmetry when the disk is geometrically thick *and* optically thick as demonstrated in Yang et al. (2017) when grains do not have large forward scattering peaks.

Since the phase function and DLP are similar for all the dust samples, we only use the XS sample for illustration. We set $\tau_0 = 10$ to increase the optical depth of the disk which allows us to compare the optically thick region near the center versus the optically thin part at larger radius. Fig. 4 shows the Stokes I, polarized intensity P, and polarization fraction p_f for three different cases described below.

Name	H_0	Scattering matrix
Model A	0.5 au	XS
Model B	5 au	XS
Model C	5 au	Rayleigh

Table 2. Column (1): The names of the models used in Section 3.2. Column (2): the value for the dust scale height H_0. Column (3): The scattering matrix sample.

We also plot the optical depth along the line of sight as contours in the top row of Fig. 4 to help diagnose the images. The names of each model and the corresponding parameters are listed in Table 2.

The left column of Fig. 4 is a model with $H_0 = 0.5$ au which corresponds to a geometrically thin disk with $H_0/R_c = 0.01$ (Model A). The p_f of the geometrically thin disk in Fig. 4g is the optically thick counterpart of Fig. 3a. A notable difference between Fig. 4g and Fig. 3a is the peak of p_f forms a ring for the optically thick case (Fig. 4g), but p_f peaks in the center of the image for the optically thin case (Fig. 3a). This is because p_f peaks where the optical depth along the line of sight is of order unity (Yang et al. 2017) which is seen in Fig. 4a. Evidently, the Stokes I, polarized intensity, and p_f do not have obvious near-far side asymmetry. The lack of obvious asymmetry is perhaps not surprising because the radiation is roughly isotropic in the midplane for this geometrically thin disk. In other words, there are a comparable number of photons that scatter at all angles to the observer for grains either in the near side or the far side.

Increasing the dust scale height can increase the radiation anisotropy (Ohashi & Kataoka 2019). Thus, in the middle column of Fig. 4, we consider $H_0 = 5$ au which is an increase of dust scale height by a factor of 10 (Model B). One can easily identify differences between the near side and far side for at least P and p_f. The near side of P (Fig. 4e) just below the center is brighter than the far side. The brightest part of P resembles a "kidney" which also appears in Yang et al. (2017). For p_f in Fig. 4h, there is a horizontal bar of $\sim 0.5\%$ (with vertical polarization) at the near side just outside the center. Additionally, the p_f at the edge of the disk for the near side (with horizontal polarization) is clearly larger than p_f (which is also horizontally polarized) at the far side.

As a comparison, we consider the same geometrically thick disk, but we use the scattering matrix in the Rayleigh limit (Model C) while adopting the same albedo and $\kappa_{\rm ext}$ as the previous cases. Similar to the Model B, the Rayleigh limit counterpart shown in the right column of Fig. 4 also shows clear near-far side asymmetry. The central regions of P in Fig. 4f also looks like a "kidney" overall with the near side being brighter than the far side. In Fig. 4i, the p_f also has a horizontal bar of vertical polarization immediately outside of the center region at the near side. However, the near and far sides of the outer region with horizontal polarization appear symmetric, which is in contrast to those in Fig. 4h. The larger levels of P and p_f (up to $\sim 12\%$) across the image is because the peak DLP in the Rayleigh limit is larger than the peak DLP of sample XS (Fig. 1b). The peak DLP in the Rayleigh limit is ~ 5 times the peak DLP of sample XS which explains the difference between the p_f images.

The polarization of the outer region of Model B is in fact due to what we expect from strong forward scattering from radiation anisotropy: the radiation from the central regions of the disk propagates to the edge and is scattered to the observer (Kataoka et al. 2015). With strong forward scattering, the near side of the disk scatters more of the polarized photons to the observer. Fig. 5 is a schematic diagram of a meridional cross section of the disk (which is an extension of Fig. 6 from Yang et al. 2017). In the optically thin regime (large radiation anisotropy), the angle between the radial direction along

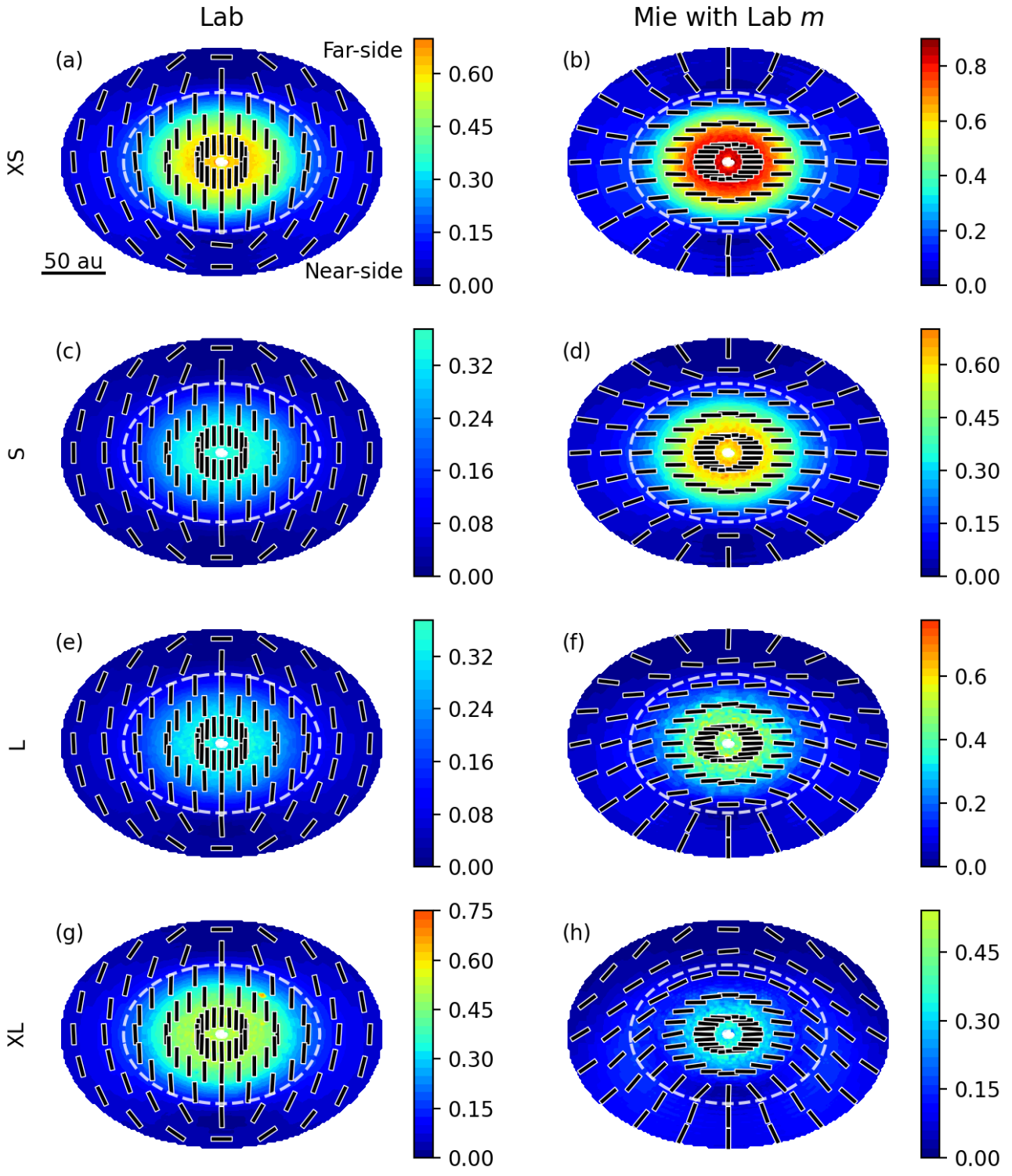

Figure 3. The images of linear polarization fraction, p_f, in percent (color maps) for different samples of experimental dust grains and their corresponding Mie calculations. The left column are produced from the experimental scattering matrix, while the right column are produced from Mie calculations. The top to the bottom row correspond to the XS, S, L, and XL samples. The polarization direction are denoted by the line segments. The dashed white contours are where the total optical depth is 0.1. The color scales are the same across images.

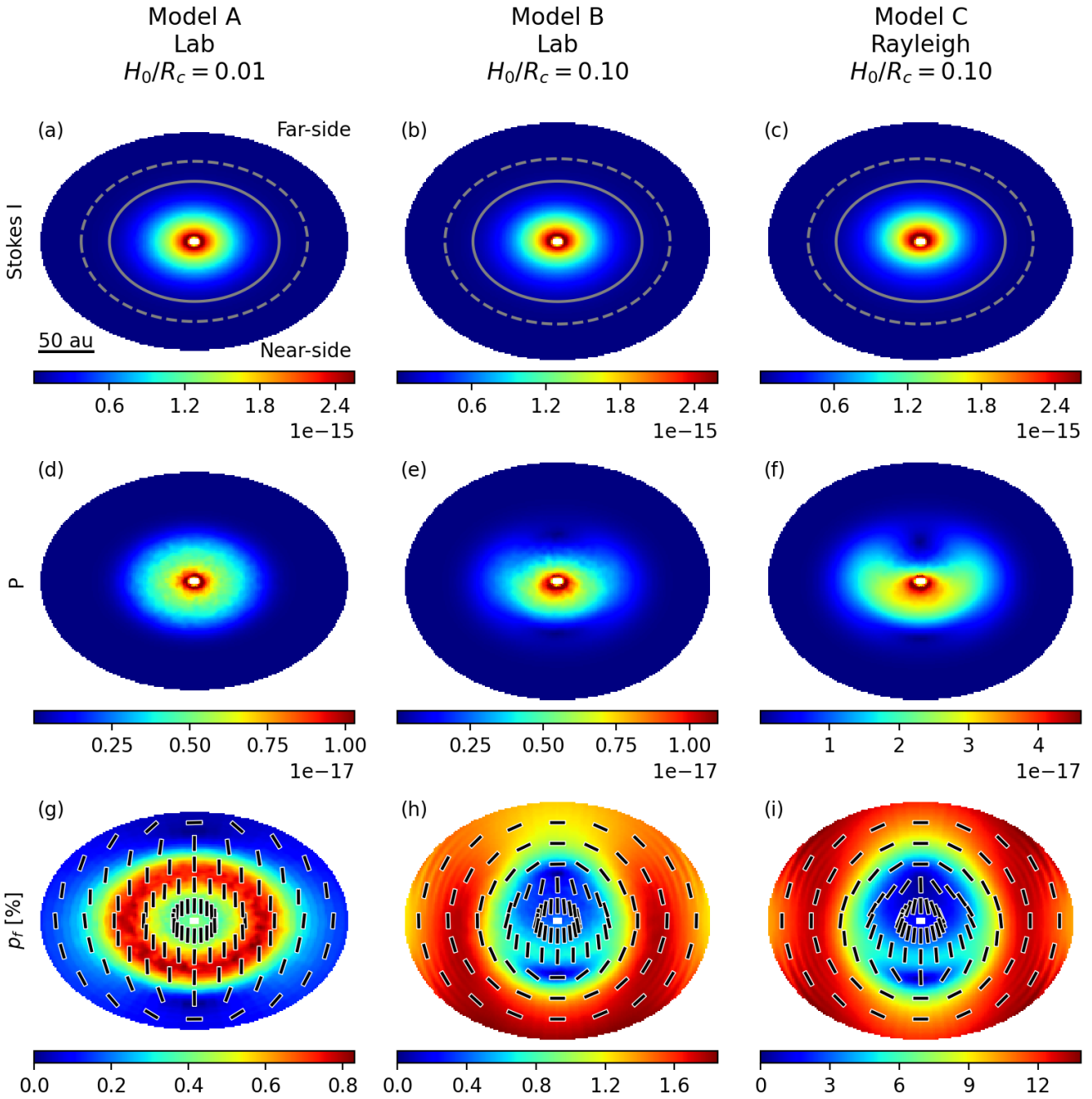

Figure 4. The polarization images for Models A, B, and C (left to right). The color map of the top row is the Stokes I, while the dashed and solid grey contours mark where the optical depth is 0.1 and 1. The second row is P. Stokes I and P are both in erg s^{-1} sr^{-1} cm^{-2} Hz^{-1}. The third row is p_f in percent with the polarization direction denoted as vectors.

the midplane to the observer is $90° - i$ for the near side. On the other hand, the far side scatters by $90° + i$. Given that F_{11} in the Rayleigh limit does not have a forward scattering peak and is, in fact, symmetric from 90°, the near-far-side asymmetry disappears in the outer optically thin region.

Both Model B and C exhibit larger P and p_f at the near side at least near the center. This is due to the disk surface effects demonstrated in Yang et al. (2017). The polarization increases with increasing inclination of the surface if the line of sight is optically thick (Yang et al. 2017). Since the local surface of the near side is more inclined than the local surface of the far side as illustrated in Fig. 5, the p_f of the near side is higher.

To examine the near-far side asymmetry in more detail, we make cuts along the minor axis and compare the near-far side profiles as a function of distance from the center. Since Stokes I is fairly similar across the near and far side, we plot the relative difference of Stokes

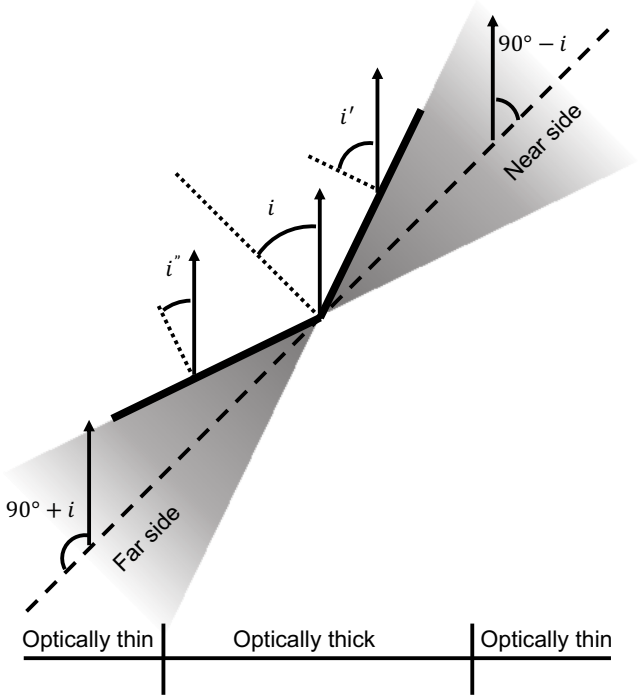

Figure 5. A schematic diagram of a cross section of the disk and its relation to the line of sight. The observer is viewing the disk from the top of the diagram. The arrows represent the direction to the observer. The disk midplane is the dashed line and the plane is inclined by i with respect to the plane of sky. The near side and far side are labeled. In the optically thin region, the scattering angle for the near side is $90° - i$, while that for the far side is $90° + i$. In the optically thick region, the surface of the disk forms an effective local inclination to the observer. The local inclination of the near side i' is larger than the that of the far side i''.

I between the near side and far side defined as

$$\Delta I \equiv \frac{I_{\rm near} - I_{\rm far}}{0.5(I_{\rm near} + I_{\rm far})} \quad (6)$$

where $I_{\rm near}$ and $I_{\rm far}$ are the Stokes I for the near side and far side respectively in the top row of Fig. 6. The second row of Fig. 6 shows the linear polarized intensity. The third row shows the polarization fraction, but we use $q \equiv Q/I$ because Stokes $U = 0$ along the disk minor axis due to the symmetry and q completely describes the polarization fraction. Using q is convenient because the sign gives the polarization direction: positive q means vertical polarization or polarization parallel to the disk minor axis for our setup and negative q means polarization perpendicular to the disk minor axis. The last row of Fig. 6 shows the total optical depth along the line of sight τ. Note that there is only one curve because τ is symmetric across the major axis for an axisymmetric disk. For clarity, we use τ' to denote the optical depth from a particular location along the line of sight to the observer.

For the geometrically thin Model A, the images in the left column of Fig. 4 show little near-far side asymmetry, and indeed the left column of Fig. 6 shows little difference between the near-far side. The more noticeable asymmetry is its P and q at the edge of the disk when $\tau < 1$. The asymmetry is similar to the geometrically thick case (Model B) which can be easily identified and understood first.

In Fig. 6b, the positive ΔI at larger radius means the near side is brighter than the far side which is less visible in the image (Fig. 4b). The positive ΔI is expected because, in the regime where radiation anisotropy is in the radial direction, photons from the near side are more forward scattered than the those from the far side. In contrast, ΔI of Model C (Fig. 6c) is near 0 at larger radius because there is no strong forward scattering.

The negative ΔI at smaller radius in Fig. 6b means the far side is brighter than the near side for Model B. As discussed in Yang et al. (2017), this is because for the same projected distance from the center, the line of sight of the far side has its $\tau' = 1$ surface is at a smaller radius with higher temperature than the line of sight of the near side (also depicted in Fig. 5). The behavior is similar to Model C (Fig. 6c) even though F_{11} is completely different. This is expected since the radiation field is more isotropic and thereby weakens the effects of differences in F_{11}. Interestingly, for Model B, the far side is brighter than the near side only by $\sim 10\%$, whereas for Model C, the far side is brighter by $\sim 20\%$. It appears that although the local surface effect dominates, forward scattering still provides some extra boost in the near side and counteracts the near-far side asymmetry from local surface effects alone.

The linear polarized intensity of Model B in Fig. 6e also has a slightly brighter near side at large radius when $\tau < 1$ (~ 1.5 times brighter that the far side). At the same time, in Fig. 6h, q of the near side is more negative than q of the far side. Both are due to forward scattering: the strong forward scattering peak consistently provides an extra amount of scattered photons that are horizontally polarized and results in an increased linear polarized intensity and extra negative q for the near side. In contrast, for the Rayleigh limit case (Model C), the linear polarized intensity in Fig. 6f and q in Fig. 6i are equal across the near side and far side as expected for large radius. At smaller radius when $\tau > 1$, both Models B and C show similar behaviors in P and q also due to a more isotropic radiation field. The larger P and q in the near side for both models are simply due to the location surface effect mentioned above and illustrated in Fig. 5.

Returning to Model A, we can identify similar features like those in Model B, but with reduced levels of asymmetry. At larger radius ($\tau \lesssim 1$), ΔI is positive which indicates a brighter near side due to forward scattering (Fig. 6a), but it is only at $\sim 5\%$ because the radiation anisotropy is much smaller than Model B. Likewise, the polarization of the near side is stronger (Fig. 6d) and horizontal (Fig. 6g). At smaller radius ($\tau >\sim 1$), ΔI is essentially zero and polarization is equal across the near and far side because the geometrically thin disk suppresses local surface effects like those shown in Model B. In other words, the disk is essentially what we would expect from an infinitely flat disk.

4 DISCUSSION

4.1 Tensions of grain size compared to the opacity index

Many sources have continuum linear polarization level that is $\sim 1\%$ at Band 7 (870μm) of ALMA and polarization is parallel to the disk minor axis (e.g. Stephens et al. 2017; Bacciotti et al. 2018; Cox et al. 2018; Hull et al. 2018; Dent et al. 2019; Mori et al. 2019). The pattern is best explained by scattering of spherical grains with size parameters smaller than but not far from unity (e.g. Kataoka et al. 2016). Thus, it appears that several disks are fine tuned to have $\sim 100\mu$m size grains.

Our results demonstrate that irregular grains alleviate the need for the $\sim 100\mu$m grains. The narrow range of grain size inferred from polarization is due to the assumption of perfectly spherical grains. As shown in Fig. 2, irregular grains with size parameters beyond 1 and

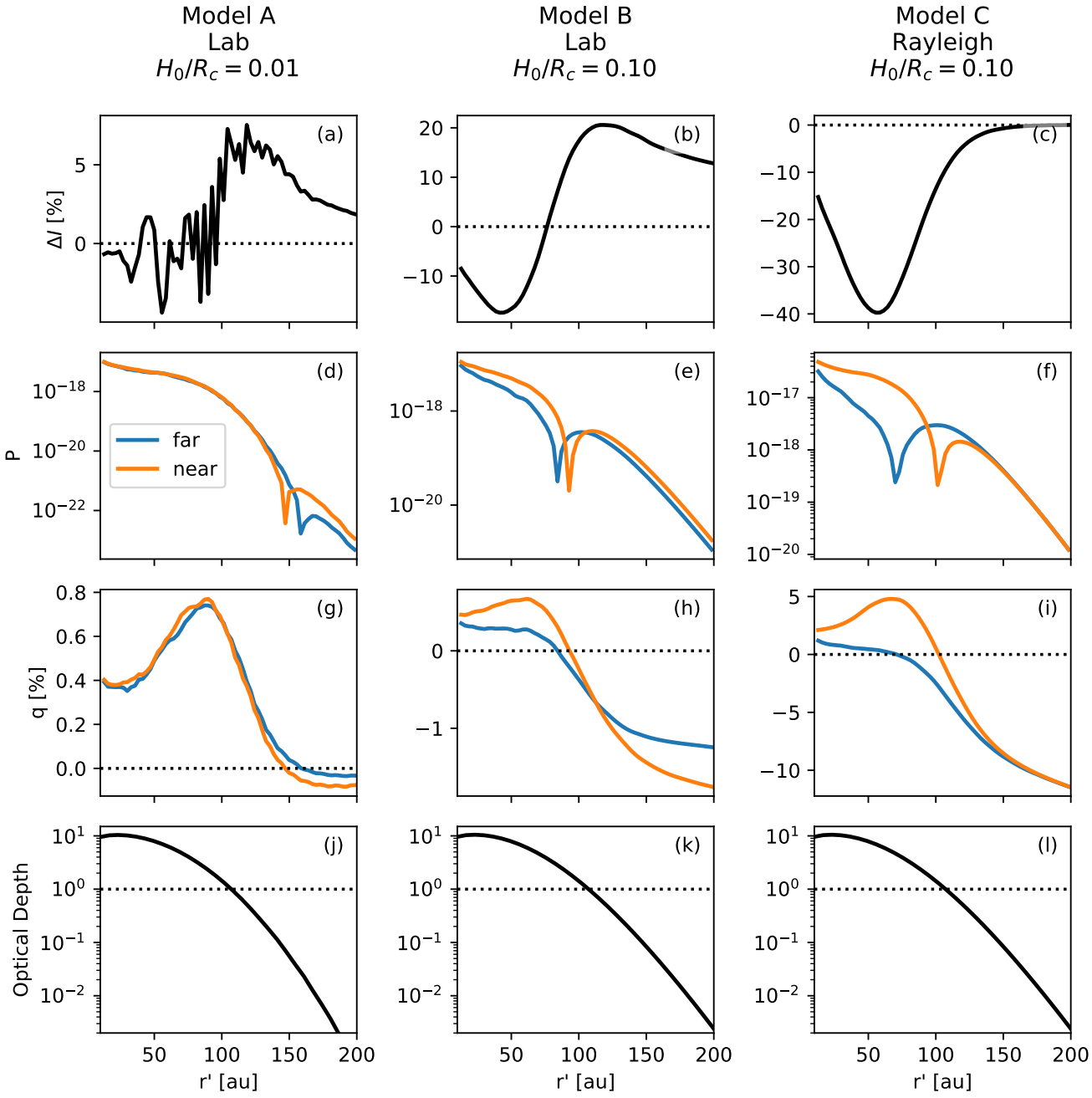

Figure 6. Cuts along the minor axis comparing the near side and the far side as a function of the deprojected radius r' in au. The columns from the left to right are Models A, B, and C respectively. The rows from the top to bottom are ΔI in percent, P in erg s^{-1} sr^{-1} cm^{-2} Hz^{-1}, q in percent, and the total optical depth. Since the optical depth is symmetric across the disk major axis, only one line is plotted. For P and q, the near side is plotted in orange and the far side is plotted in blue.

even up to 525 as for sample XL can still maintain a well-behaving polarization curve which is bell-shaped and with little to no polarization reversal. The resulting images in Fig. 3 show that these large grains can produce polarization that is parallel to the disk minor axis as compared to the Mie calculations. Thus, irregular grains prevent the strict need for $\sim 100\mu$m grains. Larger mm/cm grains, which have size parameters significantly larger than unity at (sub)millimeter wavelengths, can also produce the polarization observed by ALMA, especially for a settled dust layer that is geometrically thin.

A similar conclusion was demonstrated numerically by Tazaki et al. (2019) who calculated the scattering matrix of dust aggregates instead of solid spheres (Tazaki et al. 2016; Tazaki & Tanaka 2018; see also Kirchschlager & Wolf 2014). The resulting DLP at $\theta = 90°$ at $\lambda = 1$mm does not become negative even if the maximum grain size is 100 cm (or a maximum size parameter of ~ 6000) approximated by

the effective medium theory (Kataoka et al. 2014). A simulated disk image from Tazaki et al. (2019) also showed near-far side asymmetry in the polarized intensity and polarization fraction similar to Fig. 6. The similarity of the resulting images from both the experimental and the simulated scattering matrices for irregular grains strengthens the possibility that the observed disk polarization can be explained by scattering of large mm/cm grains, whose existence is also implied by the low values of the opacity index β.

However, it is unclear if the β index itself provides reliable measurements for grain size. The conventional relation between low β and mm/cm grains is also based on the assumption of spherical grains (e.g. Draine 2006; Birnstiel et al. 2018). β depends on other grain properties like size distribution, shape, and composition. For example, Tazaki et al. (2019) demonstrated that while the purely spherical $a_{\rm max} = 1$ cm grains have $\beta \sim 0.7$, compact dust aggregates of $a_{\rm max} = 1$ cm with a volume filling factor $f = 0.1$ still have $\beta \sim 1.5$. The β index is more related to product $a_{\rm max} f$ and not necessarily the size itself (see also Kataoka et al. 2014). Other uncertainties in deriving β include optical depth effects, alterations due to scattering, or unresolved optically thick components (e.g. Beckwith et al. 1990; Birnstiel et al. 2018; Lin et al. 2020).

Even though polarization may not pinpoint the grain size, the fact remains that polarization is caused by scattering which means that grains are at least large enough to scatter the (sub)millimeter photons efficiently which is already different from the 0.1μm interstellar grains. The level of polarization can still constrain the grain size, but not as precisely as suggested by using the polarization reversal of spherical grains (Tazaki et al. 2019). Nevertheless, the existence of scattering opens the possibility of using other attributes, such as forward scattering as demonstrated in Section 3.2, to identify grains with large size parameters. In particular, any detection of near-far side asymmetry at large radius where radiation anisotropy is prominent will indicate large grains as opposed to small grains (Section 3.2), which we leave for a future study.

From Fig. 3, we have demonstrated that adopting perfectly spherical grains can lead to drastically incorrect predictions to (sub)millimeter polarization images of disks. Given the increasing number of polarization images from ALMA and fundamental importance of grain size, there is a strong need to improve upon the polarization predictions to make the most out of the hard-fought data. An obvious method, as demonstrated in this paper, is to increase laboratory measurements. In particular, the field will benefit from measuring scattering matrices at (sub)millimeter wavelengths with materials that match the grains in protoplanetary disks as closely as possible.

4.2 Effects of the refractive index

The refractive index of $1.65 + 10^{-5}i$ in Section 3 was for forsterite at the experiment wavelength of 514 nm. Although the composition of grains in protoplanetary disks is unclear, the commonly adopted material for disks, such as astronomical silicates, are usually more absorptive at (sub)millimeter wavelengths (e.g. Draine 2003a; Birnstiel et al. 2018). Nevertheless, simulations done by Shen et al. (2009) used absorptive (e.g., silicates; Draine 2003b) and compact aggregates with size parameters greater than unity and are able to reproduce bell-shaped DLP's similar to the experimentally derived scattering matrix from forsterite (see also Zubko et al. 2009 and Tazaki et al. 2019). Laboratory results also show that large irregular grains of more absorptive material maintains the bell-shaped DLP and, in addition, the peak of the DLP increases (see e.g., Muñoz et al. 2007, Frattin et al. 2019). Thus, we can expect that irregular dust with refractive index closer to that of silicates at (sub)millimeter wavelengths would give the same qualitative results as shown in Section 3 and perhaps further increase the level of polarization for disks. That increase would make it easier to match the observations of $\sim 1\%$ polarization. The DLP's dependence on the refractive index gives a potential to constrain the composition of dust grains with polarization observations of disks. Future laboratory measurements of absorptive material with narrow grain size distributions will be extremely valuable for the study.

5 CONCLUSIONS

ALMA has consistently detected (sub)millimeter polarization that is $\sim 1\%$ and parallel to the disk minor axis for many sources. This common polarization pattern has been interpreted as evidence for scattering by $\sim 100\mu$m-sized grains (e.g. Yang et al. 2016; Kataoka et al. 2016), yet the opacity index β suggests mm/cm grain sizes (e.g. Draine 2006). In this paper, we demonstrate that the $\sim 100\mu$m sized grains inferred based on polarization is due to the strict assumption of spherical grains. We use realistic scattering matrices measured from the laboratory for irregular grains with size parameters ranging from 4 to 575 (corresponding to mm/cm-sized and even decimeter-sized grains for an observing wavelength of 1 mm) to simulate disk polarization images. Our results are as follows:

1) The degree of linear polarization (DLP) for large irregular grains (much larger than the wavelength) derived from laboratory measurements remain mostly positive, i.e., the polarization of scattered light is perpendicular to the scattering plane for incoming non-polarized light. This is similar to Rayleigh scattering except with a maximum DLP that is $10 \sim 20\%$ for all the size parameters considered. In contrast, Mie calculations using matching large spherical grains produce DLP that is negative. As a result, the experimental scattering matrices produce disk polarization that is parallel to the disk minor axis, whereas the Mie scattering matrices produce disk polarization that is parallel to the disk major axis. The inferred $\sim 100\mu$m size for spherical grains comes from the DLP becoming negative once the size parameter is larger than or order unity. By using the experimental data, we find that large irregular grains can produce polarization consistent with observations.
2) Since large grains produce a strong forward scattering peak, we find that forward scattering can create near-far side asymmetry in the disk image if the dust layer is not too geometrically thin and the disk is inclined to the line of sight. In the optically thin regions where most of the radiation travels radially outwards, the photons are more forward scattered at the near side of the disk and more backward scattered at the far side. As a result, the near side has boosted scattering with polarization that is parallel to the disk major axis. The polarization cancels with the polarization induced by inclination which is parallel to the disk minor axis. In the optically thick regions where the radiation is mostly isotropic, the role of forward scattering is minimal and the polarization fraction is larger at the near side because the local disk surface is more inclined at the near side. The degree of this near-far side asymmetry depends on forward scattering, which is a hallmark of scattering by large grains and can be used to infer their presence.

ACKNOWLEDGEMENTS

ZYDL acknowledges support from the Jefferson Foundation, NASA 80NSSC18K1095, and also support from the ALMA Student Ob-

serving Support (SOS). ZYL is supported in part by NASA 80NSSC20K0533 and NSF AST-1910106. LWL acknowledges support from NSF AST-1910364.

DATA AVAILABILITY

The experimental scattering-matrix elements as functions of the scattering angle and the size distributions are freely available at the Granada–Amsterdam light-scattering database (www.iaa.es/scattering). Also see Muñoz et al. (2021) for details of the data. Additional data underlying this article are available from the corresponding author upon request.

REFERENCES

Andrews S. M., 2020, ARA&A, 58, 483
Aso Y., Kwon W., Hirano N., Ching T.-C., Lai S.-P., Li Z.-Y., Rao R., 2021, ApJ, 920, 71
Bacciotti F., et al., 2018, ApJ, 865, L12
Beckwith S. V. W., Sargent A. I., Chini R. S., Guesten R., 1990, AJ, 99, 924
Birnstiel T., et al., 2018, ApJ, 869, L45
Bitsch B., Lambrechts M., Johansen A., 2015, A&A, 582, A112
Blum J., Wurm G., 2008, ARA&A, 46, 21
Bohren C. F., Huffman D. R., 1983, Absorption and scattering of light by small particles
Chiang E. I., Goldreich P., 1997, ApJ, 490, 368
Cleeves L. I., Bergin E. A., Bethell T. J., Calvet N., Fogel J. K. J., Sauter J., Wolf S., 2011, ApJ, 743, L2
Cox E. G., Harris R. J., Looney L. W., Li Z.-Y., Yang H., Tobin J. J., Stephens I., 2018, ApJ, 855, 92
D'Alessio P., Calvet N., Hartmann L., 2001, ApJ, 553, 321
Dent W. R. F., Pinte C., Cortes P. C., Ménard F., Hales A., Fomalont E., de Gregorio-Monsalvo I., 2019, MNRAS, 482, L29
Dong R., et al., 2018, ApJ, 860, 124
Draine B. T., 2003a, ARA&A, 41, 241
Draine B. T., 2003b, ApJ, 598, 1017
Draine B. T., 2006, ApJ, 636, 1114
Drążkowska J., Dullemond C. P., 2018, A&A, 614, A62
Dubrulle B., Morfill G., Sterzik M., 1995, Icarus, 114, 237
Dullemond C. P., Dominik C., Natta A., 2001, ApJ, 560, 957
Dullemond C. P., Juhasz A., Pohl A., Sereshti F., Shetty R., Peters T., Commercon B., Flock M., 2012, RADMC-3D: A multi-purpose radiative transfer tool (ascl:1202.015)
Escobar-Cerezo J., Palmer C., Muñoz O., Moreno F., Penttilä A., Muinonen K., 2017, ApJ, 838, 74
Frattin E., et al., 2019, MNRAS, 484, 2198
Gavino S., et al., 2021, A&A, 654, A65
Gómez Martín J. C., et al., 2021, J. Quant. Spectrosc. Radiative Transfer, 271, 107761
Harada N., Hasegawa Y., Aikawa Y., Hirashita H., Liu H. B., Hirano N., 2017, ApJ, 837, 78
Harrison R. E., et al., 2021, ApJ, 908, 141
Hu X., Wang L., Okuzumi S., Zhu Z., 2021, ApJ, 913, 133
Huang J., et al., 2020, ApJ, 891, 48
Huffman D. R., Stapp J. L., 1973, in Greenberg J. M., van de Hulst H. C., eds, IAU Symp. Vol. 52, Interstellar Dust and Related Topics. p. 297
Hull C. L. H., et al., 2018, ApJ, 860, 82
Inoue A. K., Oka A., Nakamoto T., 2009, MNRAS, 393, 1377
Iwabuchi H., 2006, Journal of Atmospheric Sciences, 63, 2324
Kataoka A., Okuzumi S., Tanaka H., Nomura H., 2014, A&A, 568, A42
Kataoka A., et al., 2015, ApJ, 809, 78
Kataoka A., Muto T., Momose M., Tsukagoshi T., Dullemond C. P., 2016, ApJ, 820, 54
Kirchschlager F., Bertrang G. H. M., 2020, A&A, 638, A116
Kirchschlager F., Wolf S., 2013, A&A, 552, A54
Kirchschlager F., Wolf S., 2014, A&A, 568, A103
Krause M., Blum J., 2004, Phys. Rev. Lett., 93, 021103
Kwon W., Looney L. W., Mundy L. G., 2011, ApJ, 741, 3
Kwon W., Looney L. W., Mundy L. G., Welch W. J., 2015, ApJ, 808, 102
Lee C.-F., Li Z.-Y., Ching T.-C., Lai S.-P., Yang H., 2018, ApJ, 854, 56
Lin Z.-Y. D., Li Z.-Y., Yang H., Looney L., Stephens I., Hull C. L. H., 2020, MNRAS, 496, 169
Lin Z.-Y. D., Lee C.-F., Li Z.-Y., Tobin J. J., Turner N. J., 2021, MNRAS, 501, 1316
Lynden-Bell D., Pringle J. E., 1974, MNRAS, 168, 603
Mori T., Kataoka A., Ohashi S., Momose M., Muto T., Nagai H., Tsukagoshi T., 2019, ApJ, 883, 16
Muñoz O., Volten H., de Haan J. F., Vassen W., Hovenier J. W., 2000, A&A, 360, 777
Muñoz O., Volten H., Hovenier J. W., Nousiainen T., Muinonen K., Guirado D., Moreno F., Waters L. B. F. M., 2007, Journal of Geophysical Research (Atmospheres), 112, D13215
Muñoz O., Moreno F., Guirado D., Ramos J. L., Volten H., Hovenier J. W., 2011, Icarus, 211, 894
Muñoz O., Moreno F., Guirado D., Dabrowska D. D., Volten H., Hovenier J. W., 2012, J. Quant. Spectrosc. Radiative Transfer, 113, 565
Muñoz O., et al., 2021, ApJS, 256, 17
Nakajima T., Tanaka M., 1988, J. Quant. Spectrosc. Radiative Transfer, 40, 51
Ohashi S., Kataoka A., 2019, ApJ, 886, 103
Ormel C. W., Spaans M., Tielens A. G. G. M., 2007, A&A, 461, 215
Pinte C., Dent W. R. F., Ménard F., Hales A., Hill T., Cortes P., de Gregorio-Monsalvo I., 2016, ApJ, 816, 25
Pollack J. B., Hollenbach D., Beckwith S., Simonelli D. P., Roush T., Fong W., 1994, ApJ, 421, 615
Sadavoy S. I., et al., 2019, ApJS, 245, 2
Sheehan P. D., Eisner J. A., 2018, ApJ, 857, 18
Sheehan P. D., Tobin J. J., Looney L. W., Megeath S. T., 2022, ApJ, 929, 76
Shen Y., Draine B. T., Johnson E. T., 2008, ApJ, 689, 260
Shen Y., Draine B. T., Johnson E. T., 2009, ApJ, 696, 2126
Sierra A., et al., 2021, ApJS, 257, 14
Stephens I. W., et al., 2017, ApJ, 851, 55
Stephens I. W., Fernández-López M., Li Z.-Y., Looney L. W., Teague R., 2020, ApJ, 901, 71
Tazaki R., Tanaka H., 2018, ApJ, 860, 79
Tazaki R., Tanaka H., Okuzumi S., Kataoka A., Nomura H., 2016, ApJ, 823, 70
Tazaki R., Tanaka H., Kataoka A., Okuzumi S., Muto T., 2019, ApJ, 885, 52
Testi L., et al., 2014, in Beuther H., Klessen R. S., Dullemond C. P., Henning T., eds, Protostars and Planets VI. p. 339 (arXiv:1402.1354), doi:10.2458/azu_uapress_9780816531240-ch015
Tobin J. J., et al., 2020, ApJ, 890, 130
Ubach C., Maddison S. T., Wright C. M., Wilner D. J., Lommen D. J. P., Koribalski B., 2012, MNRAS, 425, 3137
Villenave M., et al., 2020, A&A, 642, A164
Weingartner J. C., Draine B. T., 2001, ApJ, 548, 296
Williams J. P., Cieza L. A., 2011, ARA&A, 49, 67
Yang H., Li Z.-Y., Looney L., Stephens I., 2016, MNRAS, 456, 2794
Yang H., Li Z.-Y., Looney L. W., Girart J. M., Stephens I. W., 2017, MNRAS, 472, 373
Zubko E., Kimura H., Shkuratov Y., Muinonen K., Yamamoto T., Okamoto H., Videen G., 2009, J. Quant. Spectrosc. Radiative Transfer, 110, 1741

APPENDIX A: COMPARING TRUNCATION ANGLES

As described in Section 2.1, we adopted a truncation angle in the scattering matrix when producing the results from Monte Carlo radiative transfer. To understand the effects of truncating the forward scattering peak, we use the disk model from Section 3.1 and the phase function of the XL sample which has the strongest forward scattering. The goal is to ensure that truncating the peak allows smoother

polarization images with achievable number of photons without altering the quantitative results much. We consider three models with truncation angles θ_c at 1°, 2°, and 4° and one model without any truncation $\theta_c = 0°$.

Since truncation of forward scattering peak means considering the forward scattered photons as not interacting with the medium, the scattering opacity after truncation should be less than the scattering opacity without truncation as the forward scattering peak dominates the opacity. Note that $\kappa_{\rm abs}$ remains the same after truncation. As a reference, $\kappa_{\rm sca}$ for the different θ_c are 840, 46.7, 43.9, and 42.7 cm^2 g^{-1} respectively, and $\kappa_{\rm abs} = 1.03$ cm^2 g^{-1}.

To facilitate direct comparisons between the different models, we use $\Sigma_c = \tau_0/\kappa_{\rm abs}$ which fixes the absorption optical depth instead of the total optical depth as was done in previous sections. The benefit is that the total energy of emitted photons is kept the same and in the optically thin limit, the intensity should be the same regardless of $\kappa_{\rm sca}$. We use 10^9 photons for all the models. We show results for $\tau_0 = 0.01$ below, but we find similar differences using $\tau_0 = 0.1$.

In Fig. A1, we compare the models with different θ_c for two different cuts in the image. The first cut is along $y = 10$ au, while the other is along $x = 15$ au. For both cuts, the Stokes I, Q, U and p_f are smooth and quantitatively the same for $\theta_c = 1°$, 2°, and 4°. The model without truncation has not converged yet and the noise level for Stokes Q and U are $\sim 1-2\%$ of Stokes I. Nevertheless, Fig. A1a and b show that the Stokes I result without truncation is at the level of those with truncation.

Fig. A2 shows the images of the polarization fraction and direction for each model. Fig. A2a clearly shows a highly noisy polarization image in contrast to Fig. A2b-d. The polarization directions in the center of Fig. A2a are also messy due to the noise. The noisy region is mainly in the center where the disk is more optically thick and requires more scattering to converge.

The results are not too surprising, since the model without truncation scatters most of the photons in the forward direction which does not contribute much polarization, while the side-scattered photons that are responsible for providing polarization are rare. The necessity to truncate the forward scattering peak can be seen by comparing the total scattering opacity against the scattering opacity within the cone inside the truncation angle. The probability of photons scattered in $\theta \in [0, \theta_c]$ is

$$P(0 \le \theta \le \theta_c) = \frac{\int_0^{\theta_c} F_{11}(\theta) \sin\theta d\theta}{\int_0^{\pi} F_{11}(\theta) \sin\theta d\theta}. \quad \text{(A1)}$$

As an example, the probability of photons that scatter within 1° of forward scattering is $P(0° \le \theta \le 1°) \sim 95\%$ for the XL sample. Thus, the vast majority of photons are forward scattered and only $\sim 5\%$ of the photons can contribute to polarization.

This paper has been typeset from a TEX/LATEX file prepared by the author.

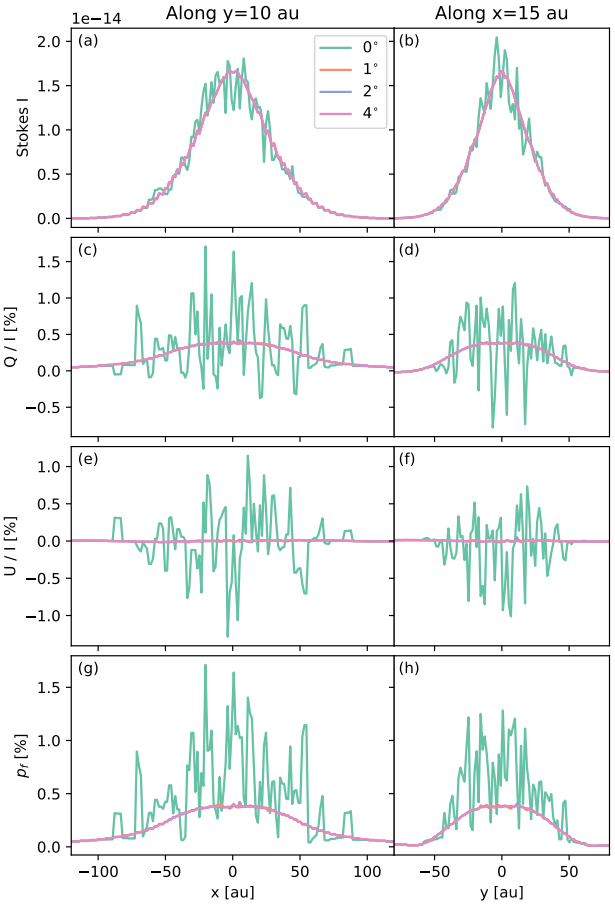

Figure A1. Comparisons of cuts along the images with different truncation angles θ_c. The panels from top to bottom are Stokes I in erg s^{-1} sr^{-1} cm^{-2} Hz^{-1}, Q/I, U/I, and p_f in percent. The left column are cuts at constant $y = 10$ au, while the right column are cuts at constant $x = 5$ au. The profiles with $\theta_c = 1°$, 2°, and 4° overlap each other given the quantitative similarities.

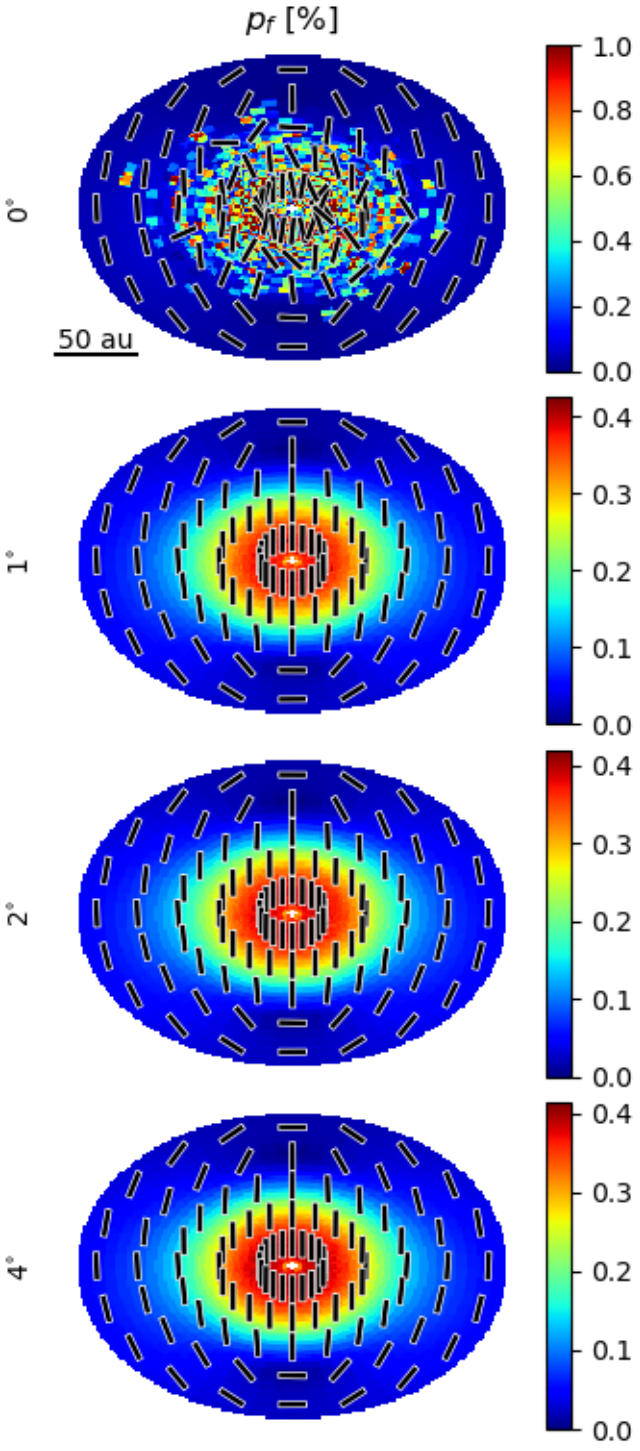

Figure A2. Comparisons of the p_f images (color maps) and its polarization angles (line segments) for different truncation angles θ_c in 0°, 1°, 2°, and 4° from top to bottom.